

Full paper

Galloping triboelectric nanogenerator for energy harvesting under low wind speed

Lanbin Zhang^{a,1}, Bo Meng^{b,1}, Yang Xia^{b,c}, Zhaoming Deng^b, Huliang Dai^{a,d,*},
Peter Hagedorn^d, Zhengchun Peng^{b,**}, Lin Wang^{a,***}

^a Department of Mechanics, Huazhong University of Science and Technology, Wuhan, 430074, China

^b Key Laboratory of Optoelectronic Devices and Systems of Ministry of Education and Guangdong Province, College of Physics and Optoelectronic Engineering, Shenzhen University, Shenzhen, 518060, China

^c School of Energy and Power Engineering, University of Shanghai for Science and Technology, Shanghai, 200093, China

^d Department of Mechanical Engineering, Technische Universität Darmstadt, Darmstadt, 64293, Germany



ARTICLE INFO

Keywords:

Triboelectric nanogenerator
Energy harvesting
Wind energy
Galloping

ABSTRACT

Energy harvesting technology of converting wind energy into available electricity is of great significance. Yet efficiently extracting wind energy at low wind speed still needs to be improved. A galloping triboelectric nanogenerator (GTENG) based on contact electrification between two flexible beams is proposed, resulting in a significant advancement of the TENG's performance under low wind speeds. The impact behavior occurs between a main beam attached with a bluff body subjected to cross flows and an auxiliary beam in the case of beyond critical wind speed. The coupled interaction between the two beams is investigated, and different contact modes have been observed. A theoretical model is constructed to further understand the working mechanism and oscillating behaviors of the GTENG. The GTENG with a 3 cm × 3 cm TENG cell achieves an output voltage of over 200V at a low wind speed of 1.4 m/s. In addition, it is meaningful that the average output power at 1.4 m/s reaches 60% of that at a relatively high wind speed of 6 m/s, which demonstrates the high output efficiency of GTENG under low wind speed. The nanogenerator's environmental adaptability is unveiled at an air-conditioner vent, indicating that the GTENG is promising to drive electric devices in outdoor environments.

1. Introduction

Ambient energy harvesting is an attractive approach to supply electricity power for distributed, portable and wearable electronics which suffer from the limited power supply of batteries and the lack of an alternative electric power supply [1,2]. To date, extensive research has been carried out to develop energy harvesting devices to capture and convert mechanical vibrations into electrical energy. Among them, electromagnetic, piezoelectric and electrostatic are typical transform mechanisms [3–9].

As one of the most common daily phenomena, contact electrification is both a familiar physical activity and a complex physical puzzle [10–13]. In the past few years, this common phenomenon has been widely investigated for energy harvesting use. Triboelectric

nanogenerators have been invented and mushroomed as a promising method of small scale energy harvesting [14–20]. The TENG works based on the effects of contact electrification and electrostatic induction, and is shown to have advantages in material availability, structural diversity and extensive applicability [21–25]. A variety of TENG devices that work under different modes have been developed and applied as power suppliers for low-power systems, such as portable electronics, wireless sensor networks, implanted biomedical devices and so on. Furthermore, TENG has been investigated as active sensors for multiple sensing uses as well. The applications of TENG for pressure detection, motion detection, humidity detection, gas sensing, ions sensing et al., have been successfully implemented [26–30].

As one of the most extensive ambient energy, wind energy is widely considered as a promising renewable and clean energy source. And it has

* Corresponding author. Department of Mechanics, Huazhong University of Science and Technology, Wuhan, 430074, China.

** Corresponding author.

*** Corresponding author.

E-mail addresses: daihulianglx@hust.edu.cn (H. Dai), zcpeng@szu.edu.cn (Z. Peng), wanglindds@hust.edu.cn (L. Wang).

¹ These authors contributed equally to this work.

already played an important role in the global power supply. Meanwhile, wind energy is also a target of concern as a considerable power source in energy harvesting [31]. TENGs were investigated for wind energy harvesting as well [32–39]. Wind-energy-harvesting TENGs with rotational structures [32] and flutter-driven structures [33–38] were developed, and quite high outputs can be achieved under a relatively high wind speed. For example, Yang et al. [33] developed a flutter-driven TENG which can capture the wind energy on the rotational structures. As a new approach for wind energy harvesting, this flutter-driven TENG works under the contact-separation mode and it utilizes simpler structure, smaller size, lighter weight and higher robustness. Bae et al. [34] reported a flutter-driven TENG based on the self-sustained oscillation of flags. Output voltage of 200 V and current of 60 μ A was achieved with a dimension of 7.5 cm \times 5 cm under a wind speed of 15 m/s. Chen et al. [35] proposed a hybrid piezoelectric and triboelectric wind energy harvester, the designed flapping-blade is subjected to wake flows and brings the PVDF to oscillate for generating piezoelectric and triboelectric voltages. The cut-in wind speed for the harvester is 4 m/s. Ravichandran et al. [36] reported an improved structure of flutter-driven TENG. It produces a peak power output of 4.5 mW under a wind speed of 5 m/s. However, among these reported works, the wind speed that can effectively drive these TENGs is usually higher than 5 m/s, but the global average near-surface (the observation altitude is 10 m) wind speed over the land is reported to be 3.28 m/s [40]. The inefficiency under low wind speed is likely to limit the applications of these TENG devices in ordinary environments.

Fortunately, mechanics orientated aerodynamic structures can be well designed to ameliorate the TENG's performance for wind energy harvesting, especially under a relatively low wind speed. Different from previous studies mainly based on flutter for triboelectric energy harvesting [33–39], in this work, a galloping structure is designed as a wind responder to improve the TENG's outputs, realizing a low wind speed of effective galloping triboelectric nanogenerator (GTENG). The designed galloping structure makes it feasible to achieve considerable oscillations to stimulate the GTENG even under a low wind speed (below 1.5 m/s), leading to a quite higher output than the previous reported work. The

theoretical model for this GTENG is constructed, and it shows a good consistency with the experimental results. In the case of a GTENG that utilizes a well-designed galloping structure with an optimized configuration, an output open voltage of over 200V was achieved under a low wind speed of only 1.4 m/s.

2. Results and discussions

The schematic of the GTENG is outlined in Fig. 1 and a contact-separation mode TENG cell attached on a Y-shape cross-section galloping structure is employed. A flat FEP membrane and a nylon membrane with porous structures on top are chosen as the friction pair in the TENG cell. The nylon membrane is pre-modified with positive charge. PET membranes serve as both substrates and insulating layer, and Al films were employed as electrodes. The photographs of a fabricated GTENG is shown in Fig. 1(b)<i>, ii> in front and top views, the size of TENG cell is 3 cm \times 3 cm. Fig. 1(b)<iii> and Fig. 1(b)<iv> respectively shows the photograph and SEM image of the Nylon membrane. The feature size of the porous structure is about 500 nm. Fig. 1(c) illustrates the setup of the GTENG's characterization in a wind tunnel, with an anemometer to measure the wind speed.

The galloping structure consists of a bluff body, a main beam and an auxiliary beam, the bluff body is attached to the free tip end of the main beam. Now that the present TENG is based on galloping responses of the main beam bringing the nanogenerator to have contact and separate behaviors with the auxiliary beam, resulting in continuous AC voltage. It's necessary to elaborate the production of fluid forces and occurrence conditions for galloping of the main beam, as shown in Fig. 2(a). When the bluff body is subjected to cross flows with wind speed of U , if transverse vibration (y direction) of the bluff body occurs and it oscillates downwards, there is a relative flow velocity (U_{rel}) between bluff body and wind flows. As a result, this relative flow velocity induces drag (F_D) and lift (F_L) forces on the bluff body. To assess the bluff body's stability, it is interested in the oscillation direction (y direction) and $dF_y/d\alpha$. In this way, the fluid-dynamic force in the y direction can be expressed as $F_y = -F_L \cos \alpha - F_D \sin \alpha$. Considering $\Delta y > 0$, then it

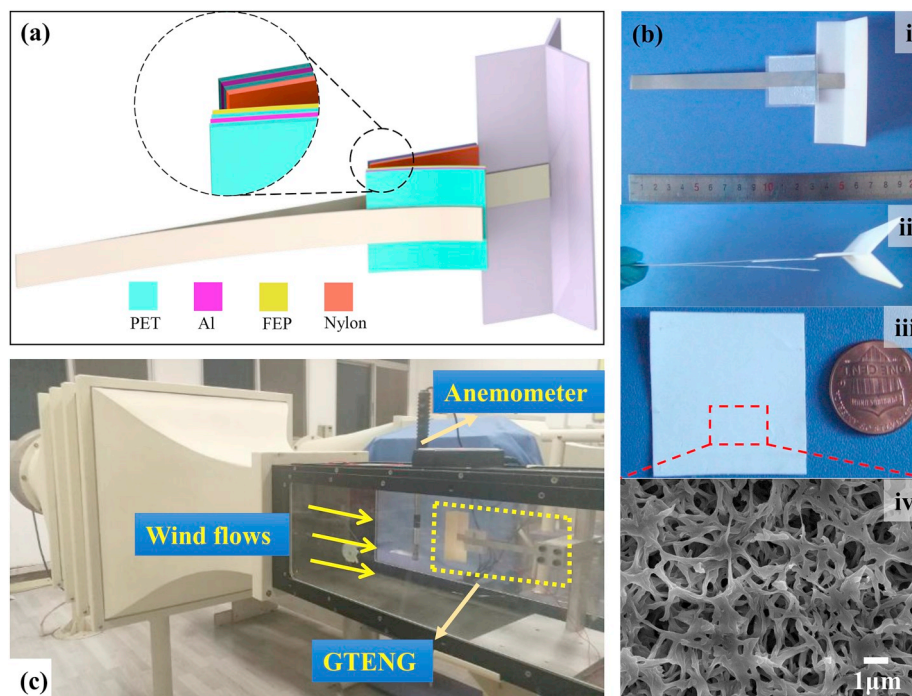


Fig. 1. (a) The schematic of the proposed GTENG. (b) Photographs of a fabricated GTENG <i> in front view and <ii> in top view; <iii> a Nylon membrane with porous structures on top as a friction layer and <iv> the top view SEM image of the porous structures. (c) The experimental setup for GTENG in the wind tunnel with an anemometer.

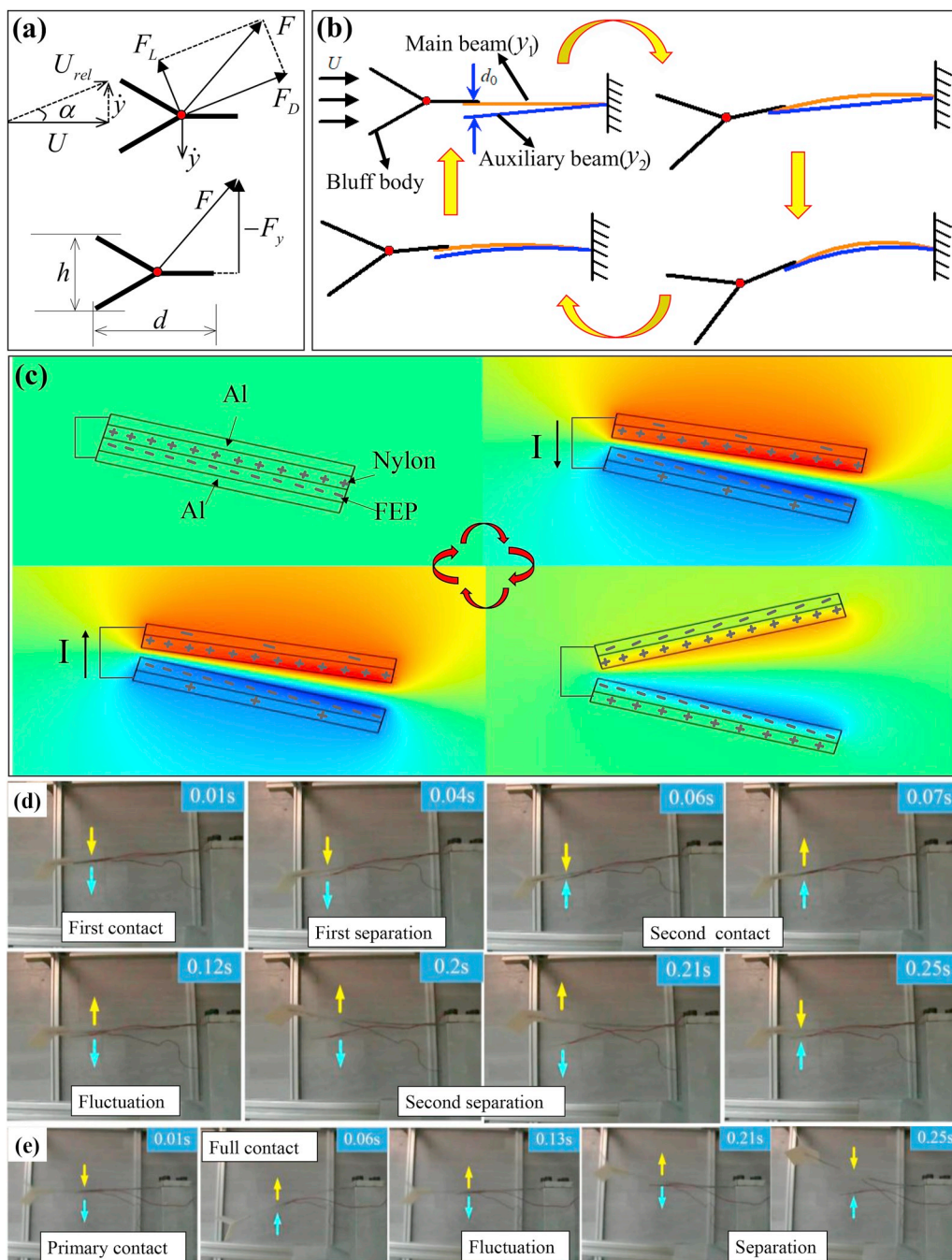


Fig. 2. The working mechanism and sequential images of contact-separation behavior of the proposed GTENG. (a) Force diagrams for cross-section of the bluff body subjected to cross-flows; (b) simplified working diagrams for the GTENG; (c) simulated diagrams for the process of charge transfer when the TENG is working; (d) double-contact mode for galloping behavior of GTENG in 12-12 configuration; (e) single-contact mode for galloping responses of GTENG in 12-9 configuration. The images were captured by a high-speed camera under a wind speed of 2 m/s.

results in $\Delta\alpha > 0$. Hence, if $dF_y/d\alpha < 0$ and $\Delta\alpha > 0$, then $\Delta F_y < 0$. According to Fig. 2(a), a positive Δy is downwards, whereas a negative ΔF_y is upwards. So they are in the opposite direction and the oscillation will decay. On the other hand, if $dF_y/d\alpha > 0$, Δy and ΔF_y will be the same direction. Then the vibration of bluff body will grow to be unstable and galloping occurs in the following. Due to existence of damping in the structure system, the onset speed of galloping is dependent on the damping and $dF_y/d\alpha$ [41].

With the help of galloping responses of the main beam, the electricity generation process in a GTENG is based on the sequence of contact-separation behaviors between two triboelectric membranes. It causes a variation of the contact and separation area between two membranes through dynamic behaviors of beams, as shown in Fig. 2(b) which is distinct from what is obtained by a flutter [34]. When the two films of Nylon and FEP are brought into contact and separate, electrons will be

transferred from the surface of Nylon film to the surface of FEP film, owing to the considerable difference in electron-attracting abilities between these two kinds of materials. Thus, the Nylon and FEP surfaces will get electrostatically charged, with positive charges on Nylon film and negative charges on FEP film. When the two charged surfaces are forced to be separated, a potential difference arises between the two induction electrodes. This potential difference will change as the charged surfaces are brought to be contacted. Under repeated separating and contact cycles driven by the wind flows, charge moves forward and back between the induction electrodes through an external load to produce continuous AC output, which is depicted in Fig. 2(c).

In fact, this operating mechanism of GTENG skillfully couples the galloping and triboelectric effect, as shown in Fig. 2(c and d) displaying sequential images of the contact-separation behaviors which are captured by a high-speed camera. In order to better capture the

vibration characteristics of the main and auxiliary beams bringing the two membranes to contact and separate with each other, the GTENG is placed at the vent of wind tunnel with a wind speed of 2 m/s for example. It is found that GTENG has two contact modes depending on the length of the auxiliary beam. Indeed, the double-contact mode occurs for GTENG in 12-12 configuration with the length of main and auxiliary beams 12 cm and 12 cm, respectively, as depicted in Fig. 2(c). The dynamic behaviors of GTENG in one period are offered. After the first contact occurs at 0.01s, the first separation shortly happens at 0.04s. Then a second contact arises later towards a shift location of oscillations at 0.06s. In the following, fluctuation of contact behavior occurs till 0.12s due to tiny relative displacement between two beams, resulting in variations of contact area between the two membranes. Finally, the second separation takes place. This arrives at state of full separation at 0.21s and starts to have a contact in the next period after 0.25s. As to GTENG in 12-9 configuration with 12 cm and 9 cm length respectively for main and auxiliary beams, it has the single-contact mode. The cycle of contact and separation is illustrated in Fig. 2(d). The oscillating main beam brings the membrane with Nylon to collide with FEP surface for a primary contact at 0.01s. Then the contact surface is increased to achieve a full contact at 0.06s. After that, there is also a fluctuation phenomenon for contact behavior. In the next, separation behavior occurs at 0.21s. It reaches to a full separation state at 0.25s with a following contact to repeat the next cycle. It should be noted that the electrostatic attraction phenomenon may exist for TENG designed in previous studies. For example, in Ref. [34], they discovered the anchoring effect (adherence) of the triboelectric sheet which is due to the electrostatic attraction between a flexible flag and a rigid plate in their flutter-driven TENG model. This is because the flexible flag almost has no stiffness and hence has no elastic restoring force. However, in our study, the triboelectric sheets are designed to attach to two flexible beams with elastic modulus of 70 GPa. The restoring force of each beam due to stiffness is enough to overcome the electrostatic attraction force. The videos of experiments for GTENG in these two configurations are offered in SI-1.

In order to further understand the process of generating the periodic voltage for GTENG in different configurations, a theoretical mathematical model is constructed in the following part. The lumped-parameter model is employed to simplify the present structure. The vibration displacements for tip of main and auxiliary beams are denoted as y_1 and y_2 , respectively. The initial space distance between two triboelectric membranes is d_0 . According to the principle of contact mode for triboelectric nanogenerator based on the theory by Niu et al. [42], the following coupled governing equations for structural and electrical models can be obtained:

when $\delta = y_1 - y_2 - d_0 < 0$, the two membranes cannot contact with each other, in this way, we have

$$m_1 \ddot{y}_1 + c_1 \dot{y}_1 + k_1 y_1 = F_y \quad (1)$$

$$m_2 \ddot{y}_2 + c_2 \dot{y}_2 + k_2 y_2 = 0 \quad (2)$$

$$R \frac{dQ}{dt} = -\frac{Q}{S\epsilon_0} \left(\frac{d_N}{\epsilon_{rN}} + \frac{d_F}{\epsilon_{rF}} + x(t) \right) + \frac{\sigma x(t)}{\epsilon_0} \quad (3)$$

while $\delta = y_1 - y_2 - d_0 \geq 0$, the contact between two membranes occurs and it has $x(t) = 0$, so we have

$$m_1 \ddot{y}_1 + c_1 \dot{y}_1 + k_1 y_1 = F_y - F_c \quad (4)$$

$$m_2 \ddot{y}_2 + c_2 \dot{y}_2 + k_2 y_2 = F_c \quad (5)$$

$$R \frac{dQ}{dt} = -\frac{Q}{S\epsilon_0} \left(\frac{d_N - \Delta d_N}{\epsilon_{rN}} + \frac{d_F - \Delta d_F}{\epsilon_{rF}} \right) \quad (6)$$

where $F_y = \frac{\rho_a A U^2}{2} \sum_{n=1,3} a_n \left(\frac{\dot{y}_1}{U} \right)^n$ is the fluid force acting on the bluff body,

which is according to the quasi-steady theory as shown in Ref. [7]. ρ_a is the mass density of the fluid, A is the front area of the bluff body and U means the wind speed. a_1 and a_3 are coefficients which are related with the onset speed of galloping and vibration displacement, respectively. m_i , c_i , k_i ($i = 1, 2$) are respectively the effective mass, damping and stiffness of the main and auxiliary beams. R is the external load resistance and Q is the electric charge. d_F , d_N and Δd_F , Δd_N are the initial thickness and strain for two dielectric membranes, respectively. S is the contact area of the triboelectric cell. ϵ_0 is dielectric constant and σ is charge density on the surface of sheet. ϵ_{rN} and ϵ_{rF} are the relative dielectric constant on two membranes. The values for the above parameters can be measured in experiments, which are given in SI-2. Indeed, Eqs. (3) and (6) are the classical V - Q - x relationship equations for the dielectric-to-dielectric TENG in contact mode [42]. The relative displacement between two dielectric membranes can be expressed as $x(t) = y_2 + d_0 - y_1$ in the present study. As to the collision force F_c which is due to the contact behavior between two membranes, it is determined based on the quasi-static assumption because the frequency of impact between two membranes is low. The collision force is assumed to be produced by the deflection of membranes. In this way, the reaction force between two membranes, namely, the collision force can be expressed as

$$F_c = E_F \frac{\Delta d_F}{d_F} S = E_N \frac{\Delta d_N}{d_N} S \quad (7)$$

where E_F and E_N are the elasticity modulus for two dielectric membranes, respectively. After some mechanics deduction the final collision force can be derived as

$$F_c = \frac{E_F E_N S}{E_N d_F + E_F d_N} (y_1 - y_2 - d_0) \quad (8)$$

Based on the theoretical modeling and identified parameters, the predicted values of peak open-circuit voltage varying with increasing the wind speed for GTENG in 12-9 configuration are compared with the measured experimental data, as shown in Fig. 3(a). The bars in experimental data curves mean the maximum and minimum values of the peak voltage at each of the wind speed. Inspecting the compared results, it is noted that very good agreement is obtained for the output voltage between the theoretical and experimental results. It is visible in Fig. 3(b) that just one contact occurs, which can be observed in experiments of Fig. 2(d). The contact area is full enough in experiments. The time history curves have been offered to show the vibration responses of the beams and the conditions (δ) for occurrence of contact behavior. Through the theoretical analysis, it is indicated that the nonlinear characteristics for dynamic responses of beams and outputs of GTENG are attributed to the combined aerodynamic and collision forces in this nonsmooth system.

To investigate the relationship between output performance and vibration behavior of the GTENG as a function of wind speed, a systematic measurement was conducted under wind speeds varying from 0.8 m/s to 6 m/s. In this case, the GTENG is in 12-9 configuration. Firstly, the open-circuit voltage (V_{oc}) for peak and RMS values varying with wind speed is shown in Fig. 4(a), indicating that there is a sharp jump phenomenon for the peak V_{oc} from about 50 V at 1.2 m/s to 200 V at 1.4 m/s. In fact, the RMS open-circuit voltage is also clearly increased in the meantime from 10 V to 40 V. This result can be explained by a striking enhancement of contact strength and hence surface contact area between two electrode poles of membranes (Nylon and FEP) with increasing the wind speed from 1.2 m/s to 1.4 m/s. As the wind speed is further increased, the peak and RMS open-circuit voltage are also gradually increased. This is because higher wind speed produces a larger vibration velocity of the main beam which further gains in strength of the surface contact force. The increased applied force will further enhance the microscale contact area between the FEP and Nylon membranes, resulting in a higher surface charge density. The corresponding micro-patterns on the surface of FEP and Nylon are shown in

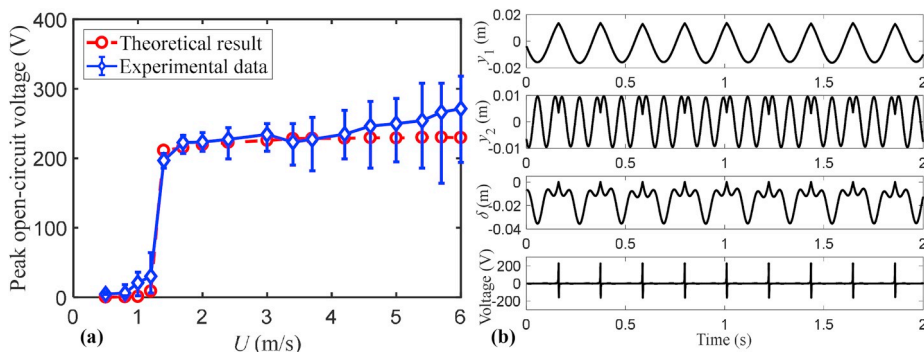


Fig. 3. (a) Comparison of peak open-circuit voltage between experimental data and theoretical result; (b) The theoretical results of corresponding tip vibration displacements for main beam (y_1) and auxiliary beam (y_2), time histories of relative displacement ($y_1 - y_2 - d_0$) and produced voltage for GTENG when the wind speed is 2 m/s.

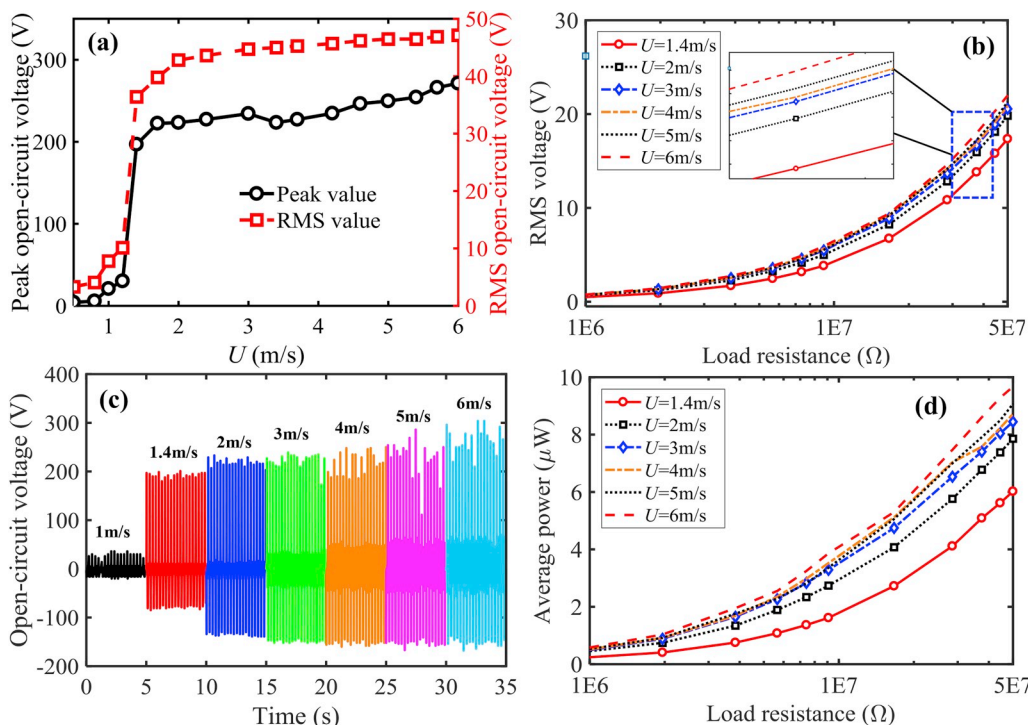


Fig. 4. Influence of wind speed and electrical load on output performance of GTENG in 12-9 configuration. (a) Open-circuit voltage as a function of wind speed for peak and RMS values; (b, d) Electrical outputs of the galloping triboelectric nanogenerator varying with load resistance in the single-contact mode; (c) Time histories of open-circuit voltage for different wind speeds; (b) RMS voltage and (d) average power.

Fig. 1(b-iv) by scanning under SEM condition. In order to further understand the output performance of GTENG with external electric load, Fig. 4(b) and (d) show the output RMS voltage and average power as a function of load resistance from $1M\Omega$ to $50M\Omega$ for different values of wind speed. Clearly, the values for output voltage and power are gradually increased with increasing the load resistance for all considered wind speeds. As the wind speed is 2 m/s, the output voltage is further increased but it almost approaches to the level of those produced by larger wind speeds (e.g. 6 m/s). This implies that the designed GTENG has an efficient output performance at low wind speeds (e.g. 1.4 m/s or 2 m/s) compared to high wind speeds (e.g. 5 m/s or 6 m/s). For instance, when the load resistance R is $50M\Omega$, the wind speed of 1.4 m/s outputs 6μ W average power which has reached 60% of the average power (10μ W) delivered at 6 m/s. This further indicates the present GTENG outputs effective power in a high efficiency at low wind speeds. The time history curves of open-circuit voltage for different wind speeds are addressed in Fig. 4(c). As the wind speed is 1 m/s, the vibration of

GTENG already occurs but the generated voltage is low. At 1.4 m/s, however, the produced voltage no matter its positive or negative peak values is jumped to a much higher value. Then the output voltage is increased smoothly followed by the increase of wind speed. This results in the variation trend of output voltage in Fig. 4(a).

Different from other types of triboelectric nanogenerator, the produced electric power in GTENG is relative to the effective contact strength and area as well as the rate of triboelectric charge separation. Therefore, understanding outputs of GTENG based on galloping-induced contact for different dimensions of main and auxiliary beams is important. In this way, Fig. 5 shows output performance of GTENG designed in other configurations by changing the length of main and auxiliary beams to outline their advantages and characteristics. Firstly, the length of main beam (L_1) is fixed to be 12 cm. The auxiliary beam is changed to be 6 cm, 9 cm and 12 cm for comparisons. The output performance in the form of peak and RMS open-circuit voltage along with vibration frequency for these three configurations (12-6, 12-9 and 12-12

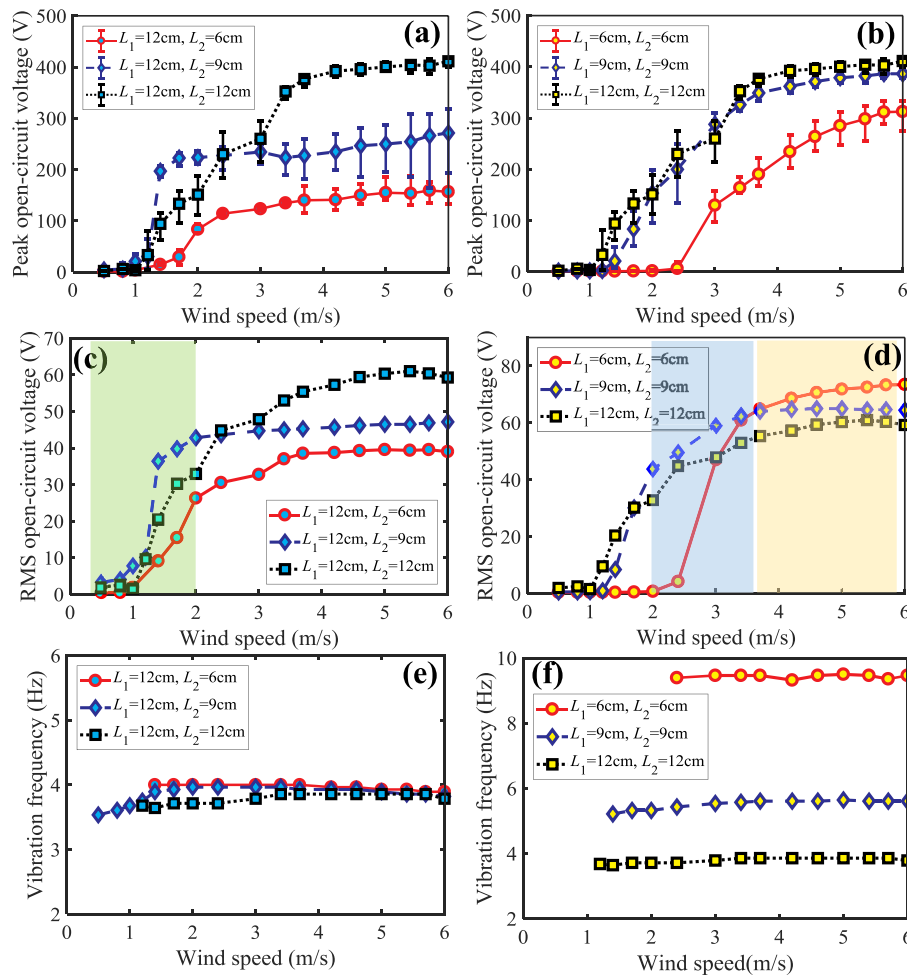


Fig. 5. Results of output performance varying with wind speed for GTENG in different configurations. (a, c, e) The length of main beam (L_1) is fixed to be 12 cm; the auxiliary beam length (L_2) is varied to be 6 cm, 9 cm and 12 cm (b, d, f) The length for main and auxiliary beams is changed at the same time to be 6 cm, 9 cm and 12 cm. (a, b) Peak open-circuit voltage; (c, d) RMS open-circuit voltage; (e, f) Vibration frequency.

configurations) of GTENG is compared with each other in Fig. 5 (a, c, e). Inspecting Fig. 5(a), these three configurations have little different values of onset speed to produce the voltage. This is because the main beam length is the same to produce the same natural frequency. According to the instability criterion, the same natural frequency and damping results in the same onset speed. The error bar means the maximum and minimum values of the measured peak open-circuit voltage in steady-state periods. It can be seen that the peak voltage is fluctuant for 12–9 and 12–6 configurations in high wind speeds but stable in low wind speeds. As to 12–12 configuration, the produced peak voltage is fluctuant at low wind speeds but stable at high speeds. GTENG in 12–6 configuration gives the lowest values of peak voltage comparing to its counterparts. However, it's better to use RMS voltage to evaluate the output performance of GTENG in these three configurations, as depicted in Fig. 5(c). Clearly, RMS voltage has the same trend as that of peak voltage varying with wind speed. This is because GTENG in these configurations almost have the same vibration frequency as seen in Fig. 5(e). In addition, it is noted that given the fixed length of main beam, it's better for the galloping triboelectric nanogenerator in 12–9 configuration as the wind speed is below 2.5 m/s and in 12–12 configuration as is beyond 2.5 m/s in order to generate higher level of output voltage. It is concluded that the threshold wind speed is mainly governed by the length of the main beam. This is because according to the theory of onset speed, when $\frac{\rho_a A U a_1}{2m} - 2\zeta\omega > 0$ the bluff body starts to oscillate and galloping occurs. ζ and ω are damping ratio and nature

frequency of the main beam attached with bluff body, which can be determined by the experiments. Then the theoretical expression for threshold speed can be obtained as $U_f = \frac{4m\zeta\omega}{\rho_a A a_1}$. Therefore, the governing parameter is mainly the nature frequency of main beam attached with bluff body, which is relative to the length of main beam (L_1). And with increasing the main beam length, the nature frequency is decreased and hence the threshold wind speed is reduced. The details of output power for GTENG in 12–12 configuration varying with load resistance are supported in SI-3. The time history curves of open-circuit voltage and short-circuit current for GTENG in 12–12 configuration at different wind speeds are offered in SI-4. Additionally, the quantity of charge that transferred during a single separation-to-contact period is evaluated through a capacitor of 100 nF without a rectifier, as its shown in SI-5. For the GTENG in 12–9 configuration, the quantity of charge that transferred during a single separation-to-contact period is 21.4 nC under the wind speed of 1.4 m/s. It reaches over 80% of the quantity of transferred charge under the wind speed of 6 m/s. For the GTENG in 12–12 configuration, the transferred charge is 29.5 nC under the wind speed of 6 m/s. That's to say, the maximum surface charge density of this GTENG is about $32.8 \mu\text{C}/\text{m}^2$.

Next, the length for main and auxiliary beams of GTENG is changing at the same time, namely, both at 6 cm, 9 cm, and 12 cm. The output performance for these three configurations (6–6, 9–9 and 12–12 configurations) is compared and shown in Fig. 5(b, d, f). It is noted that the onset speed of galloping is increased with a decrease of beam length. For

example, as the length is decreased from 12 cm to 6 cm, the onset speed is increased from 0.8 m/s to 2.5 m/s. This is because the natural frequency of main beam is increased with decreasing the length. The damping is also increased. According to the galloping instability criterion, it needs a higher wind speed to overcome the damping force to reach the occurrence of galloping vibrations. In this way, a longer beam is almost followed by a higher peak value of output voltage. This is because of a larger contact force due to the inertia effect. As to RMS output voltage, however, it has different variation trend. In particular, at higher wind speeds, GTENG in 6-6 and 9-9 configurations can produce higher values of RMS voltage. This is due to higher vibration frequencies in 6-6 and 9-9 configurations compared to 12-12 configuration, as shown in Fig. 5(f). Inspecting Fig. 5, it is concluded that when the wind speed is below 2 m/s, GTENG in 12-9 configuration has a better output RMS voltage as high as 40V. When the wind speed is between 2 m/s and 3.5 m/s, 9-9 configuration gives higher RMS voltage from 40V to 60V.

As the wind speed is beyond 3.5 m/s, 6-6 configuration is a better choice for GTENG to generate RMS voltage of beyond 60V which is much higher than other configurations.

According to Fig. 5, it is noted that GTENG in different configurations displays very different output characteristics, especially 12-9 configuration which is different from other configurations. In order to make clear of this distinct, the electrical signal in different configurations is analyzed. Taking 12-9 and 12-12 configurations for example, voltage and current measurements are carried out under a wind speed of 2 m/s for representing the single- and double-contact modes, respectively. In the single contact-separation mode, transferred charges can produce an AC output with an open-circuit voltage of 220V and a short-circuit current of 7 μ A, as shown in Fig. 6(a and b). Inspecting the profiles of electrical signal and galloping images, it is found that the contact behavior of two sheets occurs and there is an increase in contact area as seen in Fig. 6(c-I). Then the contact area is decreased with fluctuations

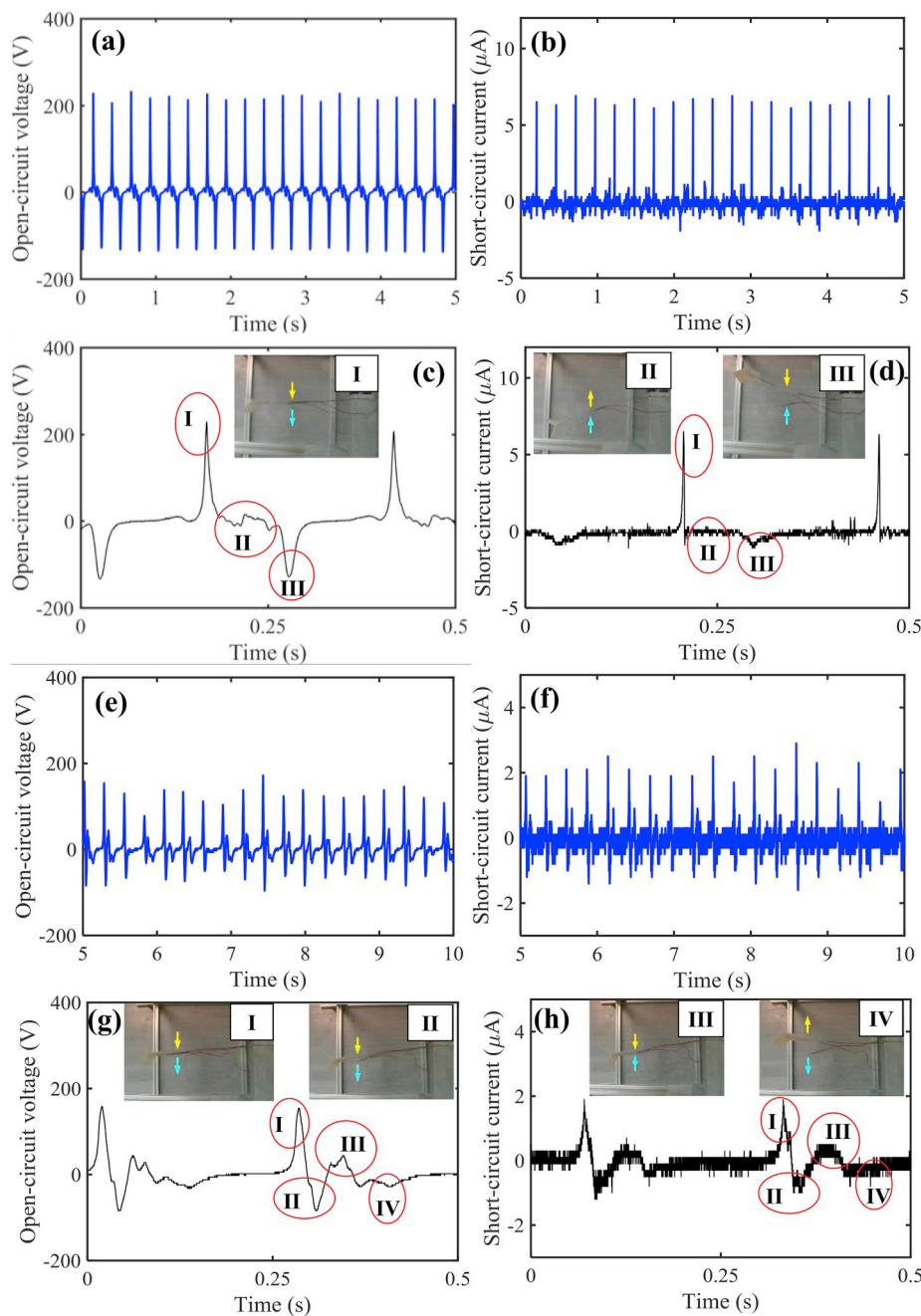


Fig. 6. Analysis of the electrical signal for single- and double-contact modes. (a–d) Electrical signal of the GTENG in 12-9 configuration subjected to a wind speed of 2 m/s. (a) Open-circuit voltage; (b) short-circuit current; (c) details in the profile of open-circuit voltage; (d) details in short-circuit current. (e–h) Electrical signal of the GTENG in 12-12 configuration under the wind speed of 2 m/s. (e) Open-circuit voltage; (f) short-circuit current; (g) details in the profile of open-circuit voltage; (h) details in short-circuit current.

(Fig. 6(c)–II), and eventual separation occurs in the following step (Fig. 6(c)–III). These oscillation behaviors clearly reflect the curves of voltage and current. A steep increase in contact area after collision between two beams is associated with the peak values of voltage and current. A fluctuation and decrease in contact area then followed by a separation are also evident in the profiles. As to the double-contact mode, two peaks of open-circuit voltage and short-circuit current in one period are shown in Fig. 6(e–h), which are the results of additional contact during vibrations at non-equilibrium position. For example, the galloping force initially drives a strong contact to produce the first peak value as seen in Fig. 6(g-I, h-I). Then the two beams soon separate due to counterforce (Fig. 6(g)–II), resulting in negative values of voltage and current. In the following, the second contact occurs at the non-

equilibrium position due to restoring force of beams (Fig. 6(g)–III). After that, the separation eventually takes place as shown in Fig. 6(g-IV). As a result, the profiles of voltage and current in electrical signal are clearly distinct from that of the single-contact mode. This additional or second contact is dependent on the beam dimensions. Indeed, with increasing the wind speed from low to high values, the contact mode is changed from single to double. As a result, there is a transition wind speed between single- and double-contact modes for different configurations of GTENG, as seen in Fig. SI-6. It is noted that with the increase of the auxiliary beam length (L_2), the transition value from single-to double-contact mode is decreased. This is because with the increase of L_2 , the vibration amplitude at the contact position is increased in the same wind speed. Then the contact behavior is more likely to happen. In

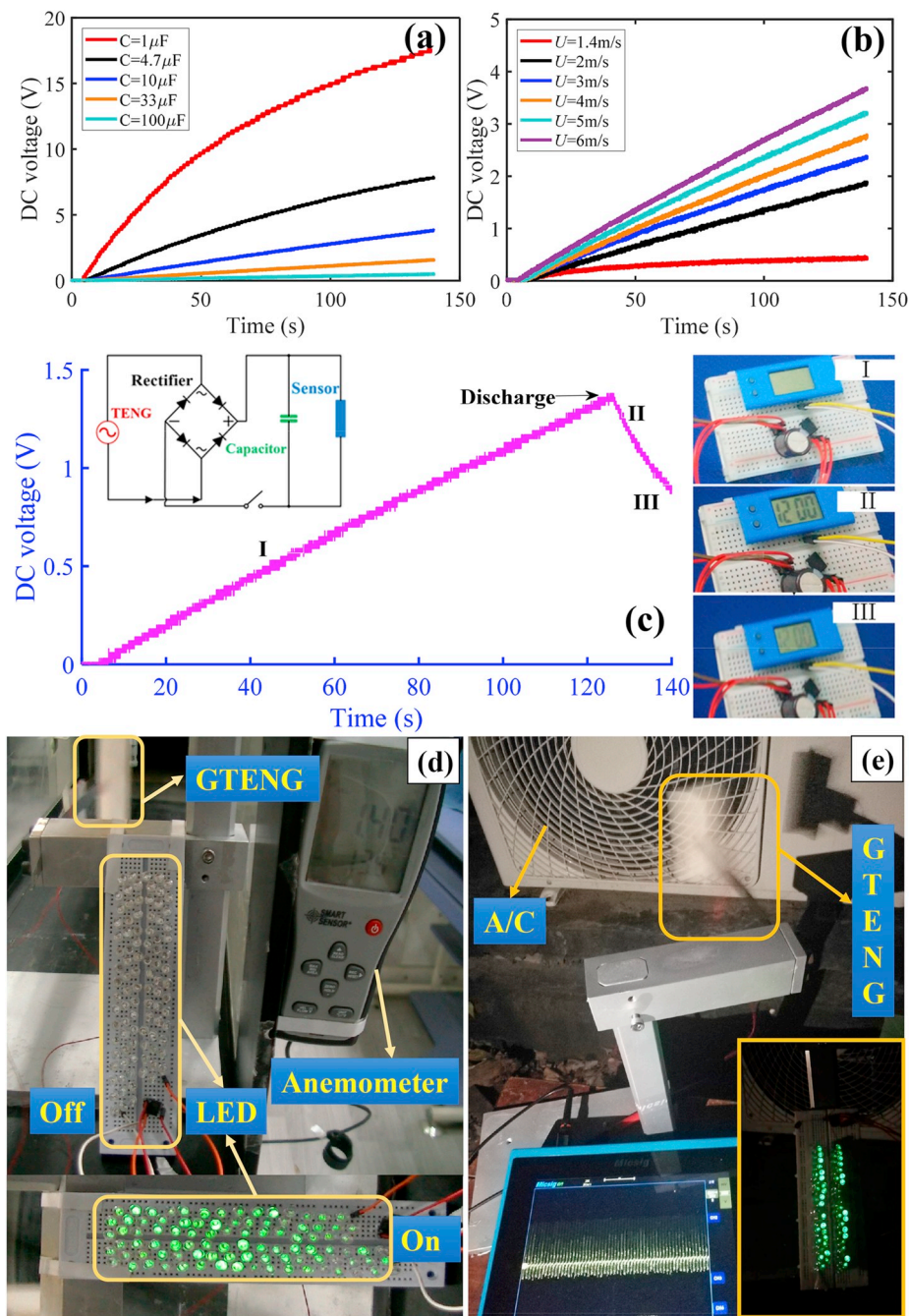


Fig. 7. Demonstrated application of the GTENG under lab and open environments. (a–d) In the wind tunnel. Charging performance of the GTENG for (a) different capacitors at a wind speed of 6 m/s, (b) 10 μ F capacitor at different wind speeds, and (c) applications in powering digital watch. Powering a number of 90 LEDs under (d) the wind tunnel environment and (e) open air-conditioner vent environment.

addition, such an additional contact due to free vibrations is a novel characteristic of the GTENG using two flexible beams. It could effectively enhance triboelectrification, especially at high wind speeds which can be figured out from Fig. 5 when the wind speed is beyond 4 m/s. This improved electrical characteristic implies a large average system power density, which can be combined with an energy storage system such as capacitors or batteries. The comparisons of output performance for the present GTENG with other recent studies [43–48] shown in Tab. 2 is offered in SI-7. It is found that whether from the aspects of output voltage or power density, the present designed GTENG is superior to most of TENGs in compared studies, especially at low wind speed conditions.

In the GTENG system, the durability of the device is indeed dependent on the property of triboelectric material due to the cyclic collision behaviors. An electrical performance is tested for prolonged galloping behaviors of the energy harvester. The open-circuit voltage is evaluated by monitoring the time of about 2 h. The results indicate that the output performance of GTENG in 12-12 configuration hardly changes as observed in SI-8. With this in mind, charging performance of the GTENG is conducted and the AC voltage is rectified to DC voltage through a rectifier circuit. The obtained DC voltage as a function of time for different capacitors is shown in Fig. 7(a) when the wind speed is 6 m/s. It is noted that the charging speed is decreased with the increase of capacitor. Clearly, increasing the wind speed from 1.4 m/s to 6 m/s is followed by an increase of charging speed, which can be seen in Fig. 7 (b). Fig. 7(c) displays the application of powering digital watch using the proposed GTENG. It is seen that after 120 s charging in step I, the DC voltage can reach to about 1.5V, then it discharges to power the digital watch at step II. It can power the digital watch to show about 20 s at step III. In order to show the GTENG can be applied at low wind speed, e.g., 1.4 m/s, 12-9 configuration of GTENG is used to do the application demonstration. In the following, a number of 90 LEDs is powered by the present GTENG in 12-9 configuration under a wind speed of 5 m/s in the laboratory as shown in Fig. 7(d). In addition, to demonstrate the performance of a GTENG in an ambient environment, it is placed at the vent of air-conditioner, as shown in Fig. 7(e). In this way, the GTENG is subjected to airflows of around 3 m/s when the air-conditioner is working. Experiments show that most of LEDs can be powered using the proposed GTENG. The corresponding experimental videos for powering LEDs are shown in SI-9.

3. Conclusions

This study presented that galloping behavior can be effectively employed for triboelectric energy harvesting at low wind speed through an elegant structure design which composed of two flexible beams. The dynamic behaviors of proposed GTENG in different configurations including single-contact and double-contact modes were identified by experimental analysis. Each contact mode resulted in a distinct characteristic for output voltage varying with wind speed, which was strongly related with the natural frequency of main and auxiliary beams. The single-contact mode for GTENG exhibited large electrical outputs at low wind speeds. With increasing the wind speed, electric performance was gradually enhanced. In the GTENG, the average output power was dependent on contact strength, surface contact area and contact frequency, in addition to the external load resistance. We demonstrated a self-sustained GTENG in 12-12 configuration generated a peak voltage of 400V at a wind speed of 4 m/s with 3 cm × 3 cm triboelectric membranes. With another design of GTENG in 12-9 configuration, the electrical performance reached 200V at a low flow velocity of 1.4 m/s. This work introduced a new route for triboelectric energy harvesting by utilizing the galloping phenomenon, which commonly happens in civil engineering but is a self-sustained vibration with low onset speed. This GTENG shows a very simple structural configuration and has the potential for large-scale applications over large areas at low cost.

3.1. Experimental methods

3.1.1. Preparing of the GTENG

FEP membrane (50 μm in thickness), Nylon membrane (GE-Amersham, RPN303B, 100 μm in thickness), PET substrates (75 μm in thickness) and Al electrodes (50 μm in thickness) were first bonded in sequence using polyacrylate adhesives. Thus, the TENG cell was fabricated. Subsequently, a Y-shape three-blade bluff body with an angle of 90° was fabricated with ABS Reins using a 3D printer. It was then fastened to the free end of the main beam, which is fabricated out of an aluminium flake. Finally, the TENG cell was fastened to the main beam and the auxiliary beam.

3.1.2. Characterization of the GTENG

A handheld oscilloscope (Micsig, TO1102) was employed to measure the output voltage with an 100:1 oscilloscope, and the short-circuit current was measured using a sampling resistor of 100 kΩ. The surface morphology on the nanostructured Nylon membrane was observed using a SEM (Hitachi, SU8010). An anemometer (SMART SENSOR AR866) is used to measure the wind speed in the experiments.

Declaration of competing interest

The authors declare that they have no conflict of interest. All procedures performed in studies involving human participants were in accordance with the ethical standards of the institutional and/or national research committee and with the 1964 Helsinki declaration and its later amendments or comparable ethical standards. This article does not contain any studies with animals performed by any of the authors. Informed consent was obtained from all individual participants included in the study.

Acknowledgments

This work is supported by the Shenzhen Peacock Team Project (KQTD20170810105439418), National Natural Science Foundation of China (Grand Nos. 11602090, 61904111, 61671308) and Alexander von Humboldt Foundation.

Appendix A. Supplementary data

Supplementary data to this article can be found online at <https://doi.org/10.1016/j.nanoen.2020.104477>.

References

- [1] Z.L. Wang, *Adv. Mater.* 24 (2012) 280–285.
- [2] S.P. Beeby, M.J. Tudor, N.M. White, *Meas. Sci. Technol.* 17 (2006) 175–195.
- [3] X.D. Wang, J.H. Song, J. Liu, Z.L. Wang, *Science* 316 (2007) 102–105.
- [4] C. Chang, V.H. Tran, J.B. Wang, Y.K. Fuh, L.W. Lin, *Nano Lett.* 10 (2010) 726–731.
- [5] L. Lin, Q.S. Jing, Y. Zhang, Y.F. Hu, S.H. Wang, Y. Bando, R.P.S. Han, Z.L. Wang, *Energy Environ. Sci.* 6 (2013) 1164–1169.
- [6] H.L. Dai, A. Abdelkefi, L. Wang, *Nonlinear Dyn.* 77 (2014) 967–981.
- [7] L. Zhao, L. Tang, Y. Yang, *Smart Mater. Struct.* 22 (2013) 125003.
- [8] P. Basset, D. Galayko, A.M. Paracha, F. Marty, A. Dudka, T. Bourouina, *J. Micromech. Microeng.* 19 (2009) 115025.
- [9] Y. Suzuki, D. Miki, M. Edamoto, M. Honzumi, *J. Micromech. Microeng.* 20 (2010) 104002.
- [10] L.B. Schein, *Science* 316 (2006) 1572–1573.
- [11] L.S. Mccarty, G.M. Whitesides, *Angew. Chem. Int. Ed.* 47 (2008) 2188–2207.
- [12] C. A. Mizzi, A. Y. W. Lin, L. D. Marks, *Phys. Rev. Lett.* 123 (2019) 116103.
- [13] S. Lin, L. Xu, W. Tang, X. Chen, Z.L. Wang, *Nano Energy* 65 (2019) 103956.
- [14] F.R. Fan, Z.Q. Tian, Z.L. Wang, *Nano Energy* 1 (2012) 328–334.
- [15] F.R. Fan, W. Tang, Z.L. Wang, *Adv. Mater.* 28 (2016) 4283–4305.
- [16] Y. Zi, S. Niu, J. Wang, Z. Wen, W. Tang, Z.L. Wang, *Nat. Commun.* 6 (2015) 8376.
- [17] G. Zhu, C.F. Pan, W.X. Guo, C. Chen, Y.S. Zhou, R.M. Yu, Z.L. Wang, *Nano Lett.* 12 (2012) 4960–4965.
- [18] X.S. Zhang, M.D. Han, R.X. Wang, F.Y. Zhu, Z.H. Li, W. Wang, H.X. Zhang, *Nano Lett.* 13 (2013) 1168–1172.
- [19] Y. Yang, H.L. Zhang, S. Lee, D. Kim, W. Hwang, Z.L. Wang, *Nano Lett.* 13 (2013) 803–808.

- [20] Q.Z. Zhong, J.W. Zhong, B. Hu, Q.Y. Hu, J. Zhou, Z.L. Wang, *Energy Environ. Sci.* 6 (2013) 1779–1784.
- [21] B. Meng, W. Tang, Z.H. Too, X.S. Zhang, M.D. Han, W. Liu, H.X. Zhang, *Energy Environ. Sci.* 6 (2013) 3235–3240.
- [22] H. Guo, X. Pu, J. Chen, Y. Meng, M.H. Yeh, G. Liu, Q. Tang, B. Chen, D. Liu, S. Qi, C. Wu, C. Wu, C. Hu, J. Wang, Z.L. Wang, *Sci. Robot.* 3 (2018) eaat2516.
- [23] R. Hinchet, H.J. Yoon, H. Ryu, M.K. Kim, E.K. Choi, D.S. Kim, S.W. Kim, *Science* 365 (2019) 491–494.
- [24] L. Cheng, Q. Xu, Y. Zheng, X. Jia, Y. Qin, *Nat. Commun.* 9 (2018) 3773.
- [25] H. Chen, Y. Song, X. Cheng, H. Zhang, *Nano Energy* 56 (2019) 252–268.
- [26] X. Cheng, W. Tang, Y. Song, H. Chen, H. Zhang, Z.L. Wang, *Nano Energy* 61 (2019) 517–532.
- [27] Y.L. Chen, D. Liu, S. Wang, Y.F. Li, X.S. Zhang, *Nano Energy* 64 (2019) 103911.
- [28] H. Yang, Y. Pang, T. Bu, W. Liu, J. Luo, D. Jiang, C. Zhang, Z.L. Wang, *Nat. Commun.* 10 (2019) 2309.
- [29] Q. Zheng, Y. Zhou, Y. Zhang, Z. Liu, B. Shi, X. Wang, Y. Jin, H. Ouyang, Z. Li, Z. L. Wang, *Sci. Adv.* 2 (2016), e1501478.
- [30] W. Tang, T. Jiang, F.R. Fan, A.F. Yu, C. Zhang, X. Cao, Z.L. Wang, *Adv. Funct. Mater.* 25 (2015) 3718–3725.
- [31] L.B. Zhang, H.L. Dai, A. Abdelkefi, S.X. Lin, L. Wang, *Appl. Energy* 254 (2019) 113737.
- [32] S. Chen, C. Gao, W. Tang, H. Zhu, Y. Han, Q. Jian, T. Li, X. Cao, Z.L. Wang, *Nano Energy* 14 (2015) 217–225.
- [33] Y. Yang, G. Zhu, H. Zhang, J. Chen, X. Zhong, Z.H. Lin, Y. Su, P. Bai, X. Wen, Z. L. Wang, *ACS Nano* 7 (2013) 9461–9468.
- [34] J. Bae, J. Lee, S. Kim, J. Ha, B.S. Lee, Y. Park, C. Choong, J.B. Kim, Z.L. Wang, H. Y. Kim, J.J. Park, U.I. Chung, *Nat. Commun.* 5 (2014) 4929.
- [35] T. Chen, Y. Xia, W. Liu, H. Liu, L. Sun, C. Lee, *J. Microelectromech. S.* 25 (2016) 845–847.
- [36] A.N. Ravichandran, C. Calmes, J.R. Serres, M. Ramuz, S. Blayac, *Nano Energy* 62 (2019) 449–457.
- [37] Z. Chen, C.B. Han, T. Jiang, Z.L. Wang, *Adv. Energy Mater.* 6 (2016) 1501799.
- [38] H. Lin, M. He, Q. Jing, W. Yang, S. Wang, Y. Liu, Y. Zhang, J. Li, N. Li, Y. Ma, L. Wang, Y. Xie, *Nano Energy* 56 (2019) 269–276.
- [39] L. Zhang, B. Zhang, J. Chen, L. Jin, W. Deng, J. Tang, H. Zhang, H. Pan, M. Zhu, W. Yang, Z.L. Wang, *Adv. Mater.* 28 (2016) 1650–1656.
- [40] C.L. Archer, M.Z. Jacobson, *J. Geophys. Res.-Atmos* 110 (2005) D12110.
- [41] M.P. Paidoussis, S.J. Price, E. de Lang, Cambridge University Press, New York, NY 10013-12473, USA.
- [42] S. Niu, S. Wang, L. Lin, Y. Liu, Y.S. Zhou, Y. Hu, Z.L. Wang, *Energy Environ. Sci.* 6 (2013) 3576.
- [43] B. Dudem, D.H. Kim, J.S. Yu, *Nano Res.* 11 (2017) 101–113.
- [44] M. Xu, Y. Wang, S.L. Zhang, W. Ding, J. Cheng, X. He, P. Zhang, Z. Wang, X. Pan, Z. L. Wang, *Extrem. Mech. Lett.* 15 (2017) 122–129.
- [45] Q. Jiang, B. Chen, Y. Yang, *ACS Appl. Energy Mater.* 1 (2018) 4269–4276.
- [46] A.N. Ravichandran, C. Calmes, J.R. Serres, M. Ramuz, S. Blayac, *Nano Energy* 62 (2019) 449–457.
- [47] Y. Bian, T. Jiang, T. Xiao, W. Gong, X. Cao, Z. Wang, Z.L. Wang, *Adv. Mater. Technol.* 3 (2018) 1700317.
- [48] Z. Quan, C. Han, T. Jiang, Z.L. Wang, *Advanced Energy Mater.* 6 (2016) 1501799.



Lanbin Zhang is a Ph.D. candidate in Department of Mechanics at Huazhong University of Science and Technology, Wuhan 430074, China. His current research interests mainly focus on vibration and small wind energy harvesting.



Bo Meng is currently an assistant professor at Shenzhen University. He received his Ph.D. degree in Microelectronics and Solid-State Electronics from Peking University in 2016. His research interest mainly focuses on micro systems and flexible electronics, especially the applications in energy harvesting and active sensing use.



Yang Xia received his Bachelor's degree in Lanzhou University of Technology, China in 2016. He is currently a graduate student in University of Shanghai for Science and Technology. His research interests include the development of self-powered system, wind energy harvesting, and application based on triboelectric nanogenerators.



Zhaoming Deng received his undergraduate degree from Hubei Engineering University, China in 2018. Currently he is a graduate student of College of Physics and Optoelectronic Engineering, Shenzhen University. His research interests are mainly focused on triboelectric nanogenerator, especially focus on the triboelectric energy harvesting devices and triboelectric tactile sensor.



Huliang Dai, Associated Professor in Department of Mechanics at Huazhong University of Science and Technology, Research Fellow of the Alexander von Humboldt Foundation. He got Ph. D. in Solid Mechanics from Huazhong University of Science and Technolgy in 2014 and then did postdoc researches in Nanyang Technological University from 2014 to 2105. His research interests are nonlinear dynamics and control, flow-induced vibrations of slender structures and energy harvesting, and underwater bioinspired robotics. He has published more than 60 SCI papers which have been cited by beyond 1000 times.



Peter Hagedorn is a Professor at Technische Universität Darmstadt, he has published more than 200 journal and conference papers. His research interests include Dynamics and Vibrations, Numerical Methods in Mechanical Engineering, Mechanical Engineering.



Dr. Zhengchun Peng received his Ph.D. degree (2010) in MEMS from the Georgia Institute of Technology. He then joined Intel as a senior R&D engineer. He is currently a distinguished professor at Shenzhen University since 2015. His main research interests focus on the fields of flexible & stretchable electronics, bio-MEMS & microfluidics, and tactile intelligent.



Dr. Lin Wang is currently the Head of Department of Mechanics, Huazhong University of Science and Technology. His qualifications include B.S. in Engineering Mechanics (2002), Huazhong University of Science and Technology, China and Ph.D. in Solid Mechanics (2006), Huazhong University of Science and Technology, China. His research interests are Flow-Induced Vibration, Nonlinear Dynamics and Control, Dynamics of Micro- and Nano-scale Structures/systems and Nonlinear mechanics of soft-material structures.